ARTICLES
PUBLISHED ONLINE: 29 AUGUST 2016 | DOI: 10.1038/NMAT4727
nature materials

Intrusion rheology in grains and other flowable materials

Hesam Askari and Ken Kamrin*

The interaction of intruding objects with deformable materials arises in many contexts, including locomotion in fluids and loose media, impact and penetration problems, and geospace applications. Despite the complex constitutive behaviour of granular media, forces on arbitrarily shaped granular intruders are observed to obey surprisingly simple, yet empirical 'resistive force hypotheses'. The physics of this macroscale reduction, and how it might play out in other media, has however remained elusive. Here, we show that all resistive force hypotheses in grains arise from local frictional yielding, revealing a novel invariance within a class of plasticity models. This mechanical foundation, supported by numerical and experimental validations, leads to a general analytical criterion to determine which rheologies can obey resistive force hypotheses. We use it to explain why viscous fluids are observed to perform worse than grains, and to predict a new family of resistive-force-obeying materials: cohesive media such as pastes, gels and muds.

The interaction of solid objects with a surrounding, plastically deforming media is a common aspect of many natural and man-made processes. In the animal world, when organisms undulate, pulse, crawl, burrow, walk, or run on loose terrain they implicitly deform their environment to produce propulsive reaction forces giving rise to their motion[1]. The physics of such interactions has been studied over a broad range of species, including aquatic organisms[2,3], small insects and lizards[4,5], as well as humans and other legged mammals[6,7]. Similar principles are used for robotic applications to design machines that run[8], fly[9], swim[10], or walk in fluids or sand[11,12]. Such complex interactions are also key to modelling vehicular locomotion on granular substrates, excavation in sand and soil[13,14], and similar problems in extra-planetary conditions[15,16]. These topics and others, including cratering dynamics and penetration in plastic solids[17,18], all depend crucially on the way local material properties produce global resistive forces on arbitrary intruders.

Inspired by a related rule-set for swimming microorganisms at low Reynolds numbers[10,19–21], a modified and wholly empirical Resistive Force Theory (RFT) for granular materials has been proposed to estimate forces on intruding surfaces moving through granular media[5,22,23]. Its use in these experimental studies show that RFT is a very strong approximation in granular media, often stronger than the corresponding version for linear viscous fluids[24]. The simplicity of the method and its effectiveness are remarkable in light of the complex constitutive properties observed of granular matter, including nonlinearity, history-dependence and nonlocality[25–29]. The method being more of a hypothesis than a theory, due to lack of a physical or mathematical explanation, new physics must be understood to explain how granular media, a complex system locally, can be explained by such a simple rule-set globally.

Herein we show that granular RFT arises as a consequence of two of the most salient mechanical features of dry granular media: a frictional yield criterion and no cohesion. A continuum theory based on these hypotheses is implemented numerically to study many two dimensional and three-dimensional (2D and 3D) intrusion cases and the results show rather conclusively that: the continuum model quantitatively predicts existing experimental intrusion data and corresponding experimental RFT input data; the continuum model reproduces the surface-level superposition rules postulated by RFT on global bodies; and by comparing to analogous viscous flow problems, the fundamental superposition concept is stronger in the granular model. Then, by performing an analysis of our continuum system, we obtain an explanation as to why the RFT approximation is so strong in granular media and why it is less so for viscous fluids. In so doing we identify new fundamental RFT formulae, which relate the experimental RFT inputs to measurable properties such as granular density, friction coefficient, and the gravitational acceleration, which could be exploited in experimentally challenging circumstances such as locomotion in micro-gravity. Our analytical approach leads to a general criterion to determine constitutive models capable of possessing a strong RFT-like reduction. To demonstrate this newfound capability, we use it to predict that purely cohesive media can also sustain a strong RFT. This is then directly confirmed using a set of full-scale finite-element simulations of intrusion in a cohesive yield stress fluid.

Background on granular resistive force theory

In recent experimental studies of arbitrarily shaped intruders moving in granular beds, it was determined that the resistive force against intruder motion is rather well represented by a simple superposition principle[23]; the intruder boundary can be decomposed into a connected collection of differential planar elements and the total resistive force is deemed equal to the sum of the resistive forces on each element as if it were moving steadily on its own. For concreteness, let us consider first the problem of an arbitrarily shaped quasi-2D intruder of thickness D buried in a granular bed; we will generalize this approach to 3D in the upcoming sections. Gravity points in the $\hat{z}$ direction, $z=0$ represents the granular surface. Formally, a surface element is on the leading surface of the intruder if a ray along its velocity vector does not intersect another point on the surface. For any subset S of the leading surface, RFT is defined by the claim that when the body is moving in the xz-plane the resistive force (f_x,f_z) on S is well approximated by

$$(f_x,f_z)=\int_S \left(\alpha_x(\beta,\gamma),\alpha_z(\beta,\gamma)\right) H(z)\, z\mathrm{d}S \qquad (1)$$

Massachusetts Institute of Technology, 77 Massachusetts Avenue, Cambridge, Massachusetts 02139, USA. *e-mail: kkamrin@mit.edu

where β is the orientation angle (attack angle) of the differential surface element and γ is the angle of the velocity vector (intrusion angle) of the element, both measured from the horizontal. The key ingredient in RFT is the selection of the functions α_x and α_z, which is done experimentally from force data for small intruding flat plates under various γ and β conditions. The term $H(z)z$, for H the Heaviside function, removes resistive force above the free surface and increases the resistance linearly with depth.

The effectiveness of equation (1) is unexpected for many reasons. At first glance, it appears to be motivated by the assumption of a lithostatic pressure distribution, $P=\rho gz$, surrounding the moving intruder. However, this assumption is strongly incorrect. DEM simulations of buried granular intruders[30], experimental data[31], as well as our own simulations (see Supplementary Methods) contradict this assumption rather significantly. Experiments show the stress on a moving intruder deviates from lithostatic by as much as a factor of 15 in granular media[31]. The deviation from a linearly varying pressure field is pronounced everywhere the material is moving[31], and continues over a distance into the static zones (for example, Supplementary Methods, Supplementary Fig. 2). Additionally, the superposition property of equation (1) assumes that the force on a segment of the leading surface depends only on its position, orientation and motion direction, with no cross correlation of resistive forces whatsoever between the different segments. This is a significant unproven assumption and the major source of simplification in RFT. The strength of this assumption in grains is unexpected in light of the more de-localized nature of force and motion in other materials; in viscous fluids, for example, the Stokes boundary integral formula requires that the motion at any point on a submerged surface depends on the resistive force distribution over the entire surface, weighted inversely by distance. For these reasons, the surprising accuracy of equation (1) in practice has remained an open physical question since its introduction.

Frictional-plastic rheology

To obtain deformation and stress within a continuous body of grains, we consider a constitutive behaviour in line with the following three basic assumptions: first, we assume a constant internal friction coefficient, μ_c, to relate the scalar shear stress and pressure during plastic flow. Second, we assume a rapid approach to the critical state of volume-conserving flow[25]—granular dilation is typically only a few percent regardless—such that plastically flowing and rigid media are assumed to be at some close-packed density, ρ_c. Third, we append an 'opening behaviour' that lets material expand volumetrically (that is, lets $\rho<\rho_c$) when an element attempts to enter a state of tension, to model the cohesionless granular disconnection response. Open states often occur in the wake of a moving intruder, before material from above collapses back down to ρ_c, as discussed in the Supplementary Section 1 in detail. The bare-bones model we propose, with ρ_c and μ_c as the sole parameters, does not account for rate-sensitivity, evolving strength/porosity during flow, fabric anisotropy, or nonlocal effects based on particle size, which are all known to exist. The mathematical details of this model, which we shall refer to as frictional plasticity, are given next. Supplementary Section 3 provides a discussion of the possible relevance of the other modelling complexities just mentioned.

Details of the continuum approach

The strain-rate tensor is defined from the spatial velocity field, v_i, by $D_{ij}=(\partial v_i/\partial x_j+\partial v_j/\partial x_i)/2$. We define the scalar (equivalent) shear rate as $\dot{\gamma}=\sqrt{2D'_{ij}D'_{ij}}$, where $D'_{ij}=D_{ij}-\delta_{ij}D_{kk}/3$ is the strain-rate deviator and δ_{ij} is the Kronecker delta. Assuming that the Cauchy stress, σ_{ij}, is co-directional with the strain rate, and that the Drucker–Prager yield criterion is satisfied during yielding, we write

$$\sigma_{ij}=-P\delta_{ij}+2\mu_c PD'_{ij}/\dot{\gamma} \quad \text{if } \dot{\gamma},P>0 \tag{2}$$

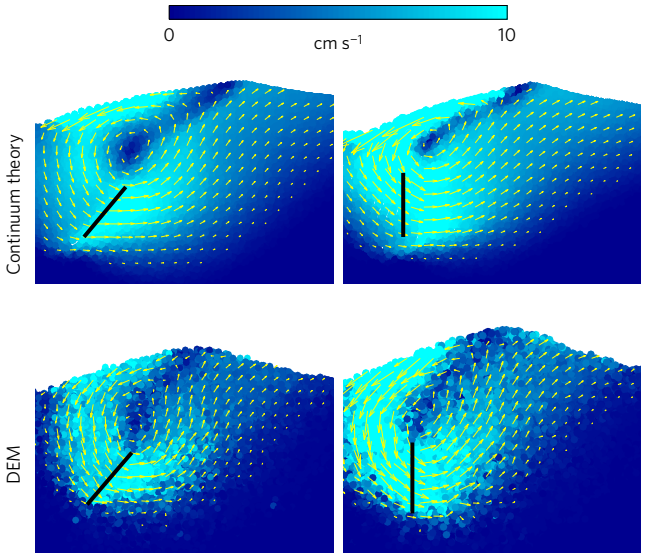

Figure 1 | Theoretically predicted intrusion flow fields. Speed distribution (contours) and velocity directions (arrows) created by motion of a submerged flat intruder moving rightward at 10 cm s^{-1} at two sample orientations. Results from the continuum theory (top) and DEM simulations from the literature[22] (bottom).

In the above, $P=-\sigma_{kk}/3$ is the isotropic pressure. Whenever $\dot{\gamma},P>0$, we assert incompressible plastic flow ($D_{kk}=0$) such that the density of the packing remains at ρ_c. Whenever $\rho<\rho_c$, we set $\sigma_{ij}=0$ to represent granular disconnection. Momentum balance, $\partial\sigma_{ij}/\partial x_j+\rho g_i=\rho\dot{v}_i$, closes the system of equations, where g_i is the acceleration of gravity and the superscript dot represents the material time derivative.

To provide stresses in rigid zones, where $\dot{\gamma}=0$ and $P>0$, and to aid in implementing the above pressure and flow constraints numerically, we admit a small elastic strain component to the deformation[32]. See Supplementary Section 1 for more details. As long as the elastic stiffness is sufficiently high, the observed plastic flow behaviour is unaffected and approaches a rigid-plastic solution, a point we verified directly in our simulations.

We numerically implemented the model in 3D using a custom material model in the finite-element package Abaqus/Explicit[33] (see Supplementary Section 1, for details; material definition code is also available as a supplementary file). We first consider problems with plane-strain symmetry before considering general cases. No-penetration conditions are applied at the sides and bottom of the bed, and the free surface is pressure-free. Gravity is gradually ramped up to its final value before intruder motion begins. The intruding object is represented as a fully rough, thin object. Sample flow directions and velocity distributions for a plate intruder obtained numerically by the continuum theory are shown in Fig. 1 and compared to DEM results in the literature for the same geometry, having similar density and internal friction[22]. It is worth noting that even though our intruder boundary condition assumes a fully rough interaction, which is an inexact representation of the condition assumed in the DEM simulation, the positive comparison suggests this difference is not crucial.

Results from the continuum theory

To establish a potential connection between frictional plasticity and RFT, we begin by simulating a flat intruder moving under many attack angles β and intrusion angles γ ($-\pi/2<\beta,\gamma<\pi/2$) to obtain predictions for the resistive force plots (RFPs) of α_x and α_z. For each angle pair, the drag and lift forces acting on the plate are extracted when plastic flow is well-developed. To compare RFPs,

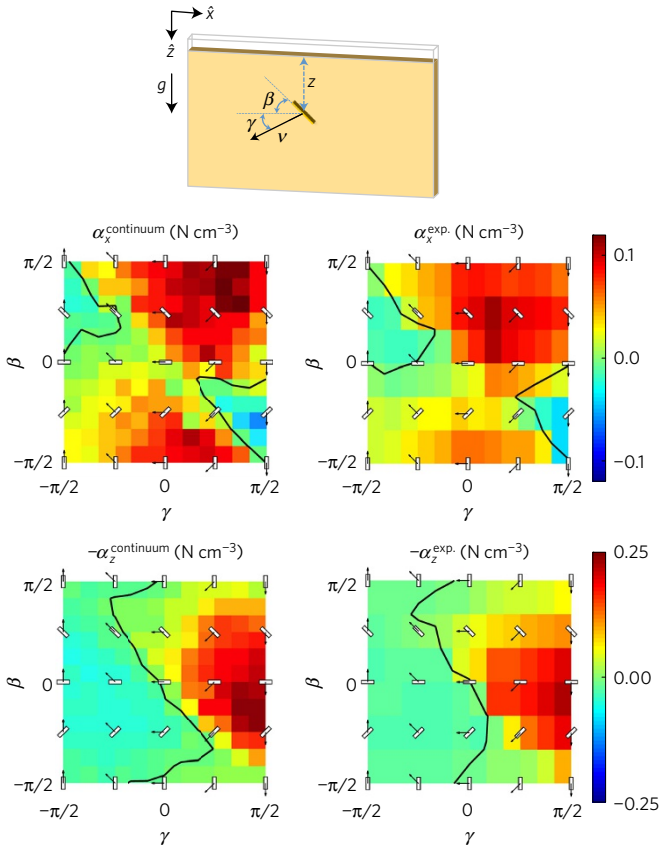

Figure 2 | Theoretically predicted versus experimentally obtained resistive force plots. RFPs obtained from frictional plasticity simulations ('Continuum' superscript), compared against published experimental RFPs[5] ('exp.' superscript) for a media composed of glass beads. Resistance coefficients in the x and z directions are α_x and α_z, respectively, and γ and β are the intrusion angle and attack angle, respectively. We show $-\alpha_z$ for consistency with plot conventions used in ref. 5. Solid black lines show the zero values. The intruder depth is z and g is the acceleration of gravity, oriented downward.

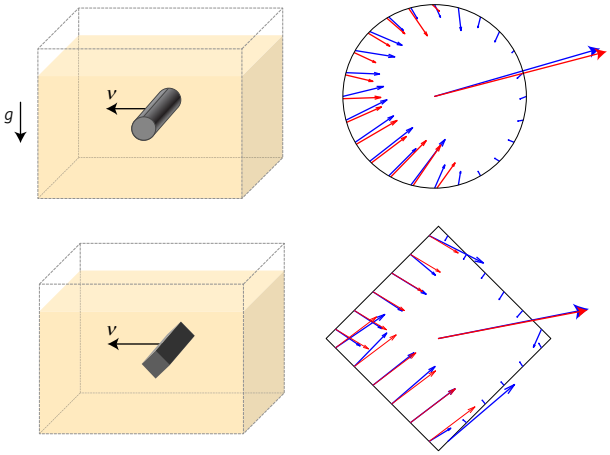

Figure 3 | Demonstration of the superposition principle arising from the continuum model. Distribution of force on the perimeter of two long moving objects as calculated directly from simulations of our continuum theory (blue arrows), compared to predictions from RFT using theoretical RFPs from Fig. 2 (red arrows). Net resistive force shown at the centre of the object; the two models give nearly indistinguishable results. Intruders move horizontally with speed v. Gravity, g, is oriented downward.

we fit our continuum model parameters (μ_c and ρ_c) from reported properties of loose packed 0.3 mm glass beads[5]. As shown in Fig. 2, computed RFPs of α_x and α_z are strikingly similar to the experimentally obtained RFPs for glass beads[5]. The only noteworthy difference between the two sets of figures is in the location of maximum drag force, which could be attributed to the oversimplification of assuming a no-slip intruder boundary condition. We reiterate that no fitting parameters were used in the constitutive model, only the reported repose angle and density of the experimental material[5].

When the shape of the intruder is changed from plates to more arbitrary selections, we find the resistive forces obtained from the continuum theory comply very well with the superposition principle of RFT. For instance, in Fig. 3, the force distribution and resultant forces on circular- and diamond-shaped intruders are obtained directly from finite-element implementation of the frictional-plastic model. The forces are then compared with the corresponding RFT predictions, which use the model-generated RFPs shown in Fig. 2. Although some errors are observed at the edges, the force distributions from both methods show a good match, and resultant force vectors show a near-perfect correlation. This observation suggests that the deviations in force distributions may be due to numerical variations in the explicit finite-element implementation of the theory.

Equation (1) can be extended naturally to general 3D cases, to include a non-trivial out-of-plane dimension; experiments[5] have verified that surfaces whose shapes vary in the y direction also maintain the superposition principle. To assess the generality of the RFT superposition principle in 3D, we employ our model to study forces on a sequence of buried V-shaped intruders. Because RFT is supposed to apply only to the leading surface of an intruder, we limit our attention to an obtuse V geometry, with apex angle fixed at $\theta_V = 135°$, in which most orientations of the V admit both wings to be part of the leading surface.

We consider both vertically and horizontally aligned cases for the intruder orientation, varying the orientation angle φ of the submerged V over many values, where φ denotes a pitching angle (in the vertical case) or yawing angle (in the horizontal case), see diagrams in Fig. 4. For each orientation, we impose rightward motion of the V intruder, and record the 3D vector of resistive force that arises on the intruder at steady state. Then we run two new simulations, one for each wing of the intruder moving by itself, where the wing is simulated as a single plate maintaining the same exact alignment, positioning and motion that it had when it partook in the group V motion. If RFT superposition holds, the sum of forces in the latter two tests should equal that of the full V test. In Fig. 4b we perform the same sequence of tests, but assume instead a zero-Reynolds viscous fluid for the surrounding media, simulated using a similar finite-element code. All cases engage considerable drag force in the direction of motion, as expected. The vertically aligned intruders experience vanishing F_y due to symmetry, and F_z switches sign at certain orientations due to the ploughing action of the intruder movement, similar to the oscillatory nature of the y-force for the horizontal intruder. In the horizontal case, unlike the zero viscous F_z force, the intruder in the frictional plastic bed experiences an F_z force that on average pushes upwards, demonstrating the well-known drag-induced lift effect[22] in granular systems.

The comparison in Fig. 4a shows that superposition works extremely well in frictional plasticity for all force components. The agreement is roughly in the same range as the deviations observed in past granular RFT experiments[22,34]. In the ranges indicated in grey, the leading-surface assumption of RFT is violated; that is, one plate is behind the other. The agreement is not as strong in these zones, but still overall good. For this 3D study there are no analogous experimental tests in the literature to verify the findings of the theory. The error of the RFT force prediction, $|\mathbf{F} - \mathbf{F}_{\text{RFT}}|/|\mathbf{F}|$, is found to be 7.3% averaged over all orientations of the V and

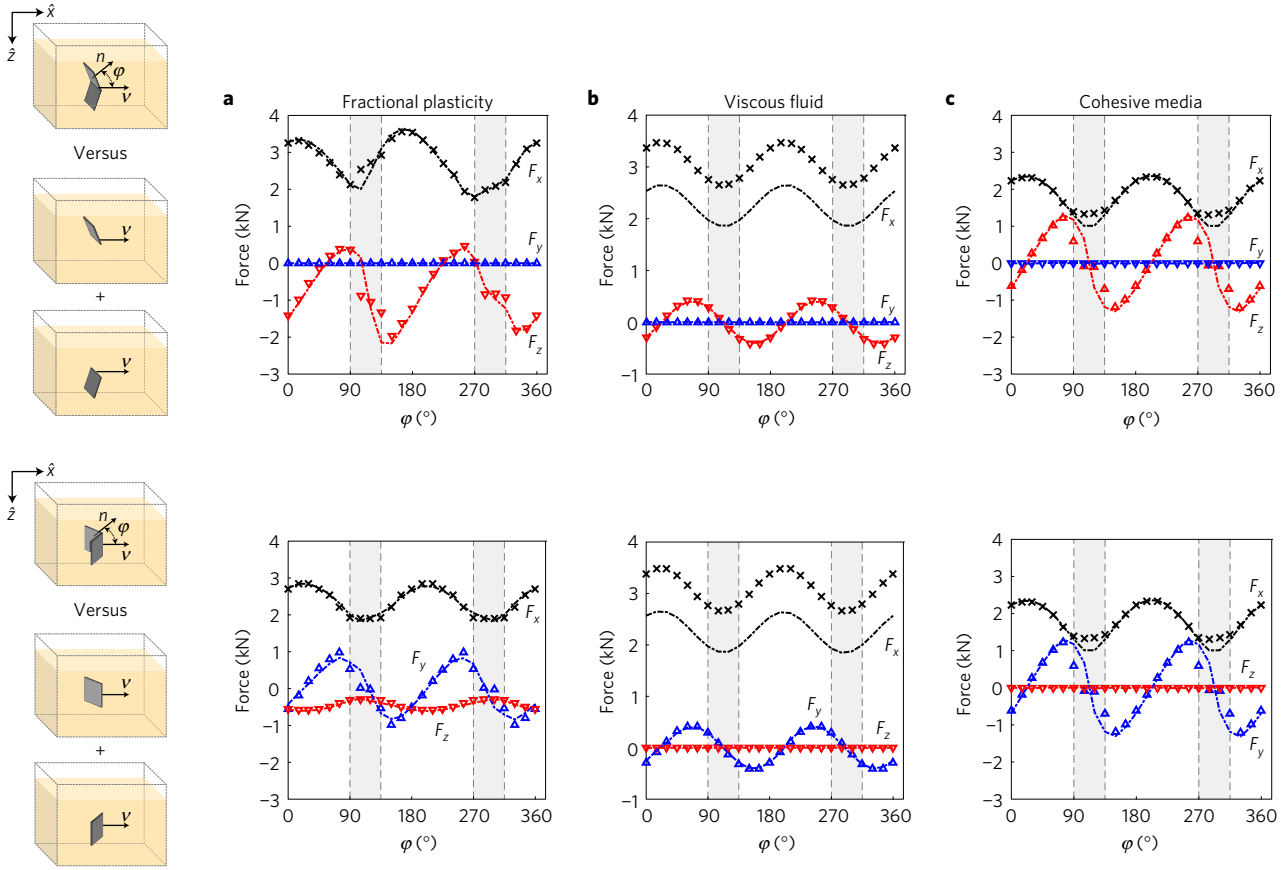

Figure 4 | Validity check for superposition in 3D. The drag force, F_x (crosses), and the components of downward force, F_z (red coloured downward triangle), and lateral force, F_y (blue coloured upward triangle), acting on a submerged 'V' intruder moving rightward with speed v at various orientation angles, φ, with respect to the intruder motion. Vertical (top row) and horizontal (bottom row) intruder alignments are both tested. Gravity g points down. Dashed lines show the corresponding forces obtained by superposition from isolated, individual-wing tests. Rheology of the surrounding media: (**a**) Frictional plasticity ($\rho_c = 4\,\mathrm{g\,cm^{-3}}$, $\mu = 0.4$); (**b**) Zero-Reynolds viscous fluid ($\eta v = 15\,\mathrm{N\,m^{-1}}$); (**c**) Purely cohesive media ($\tau_y = 10\,\mathrm{kPa}$). Intruder consists of two square plates of side length 20 cm. Grey regions indicate orientations violating the leading-edge assumption of RFT.

3.9% when orientations that violate the leading-surface assumption are excluded.

In contrast, the superposition force in a viscous fluid half-space has a considerable error in the drag direction, as shown in Fig. 4b, which is the largest force component. The total error of the force vector is about 36% averaged over all orientations. The non-trivial component in the lateral direction actually seems to show a good degree of superposition, but this may be a coincidence; when the apex angle of the V is varied, the disagreement becomes more pronounced. In the presumably simpler case of $\theta_V = 180°$, that is, a flat intruder, the error of viscous superposition has significant values in this component too, leading to an average error of 42%, while the superposition of the frictional model maintains its accuracy, with an average error of about 4.6% (see Supplementary Section 4).

Analytical explanation

The results thus far have demonstrated numerically that RFT hypotheses emerge strongly from the continuum equations of frictional plasticity. To provide an explanation as to why these equations replicate RFT and to predict if other materials have a strong RFT collapse, we study the behaviour of resistive forces in a simple family of geometries reminiscent of a 'garden hoe'. Exact solutions to the continuum plasticity system are highly non-trivial to obtain, but in this geometry many results can be inferred using dimensional analysis without having to solve the differential equation system.

Consider a semi-infinite half-space of frictional continuum media (see Fig. 5). Suppose a large square-shaped intruder with edge length L is inserted into the media at angle β from the horizontal. Its top edge remains coincident with the free surface. The intruder is translated at a speed v in a direction angled γ from horizontal, producing an assumed quasi-static motion of the material. The total resistive force $\mathbf{F}_{\mathrm{gran}}$ on the intruder is then calculated from the continuum model. Due to the parameters of the model, the force can depend only on β, γ, L, μ_c, the weight density, $\rho_c g$, and perhaps a wall friction coefficient between the intruder and the material, μ_w. Define L, L/v and $\rho_c g L^4/v^2$ as units of length, time and mass, respectively. Non-dimensionalizing, we find that $\mathbf{F}_{\mathrm{gran}} = \rho_c g L^3\, \boldsymbol{\Psi}_{\mathrm{gran}}(\beta, \gamma, \mu_c, \mu_w)$. Redefining $\boldsymbol{\Psi}_{\mathrm{gran}}$ by absorbing the material constants, we have

$$\mathbf{F}_{\mathrm{gran}} = L^3\, \boldsymbol{\Psi}_{\mathrm{gran}}(\beta, \gamma) \tag{3}$$

To approximate the same force using RFT, one first computes RFPs of α_x and α_z by gathering data on the intrusion of a small plate of edge length $\lambda \ll L$. The above formula can be applied to the small plate, and the result is that the RFPs must obey $(\alpha_x(\beta,\gamma), \alpha_z(\beta,\gamma)) = 2\boldsymbol{\Psi}_{\mathrm{gran}}(\beta,\gamma)/\sin\beta$. We then check the RFT superposition principle by integrating equation (1) over the surface, S, of the $L \times L$ garden hoe to obtain

$$\mathbf{F}^{\mathrm{RFT}}_{\mathrm{gran}} = \int_S \left(\alpha_x(\beta,\gamma), \alpha_z(\beta,\gamma)\right) z\,\mathrm{d}S$$

$$= \int_S \left(2\boldsymbol{\Psi}_{\mathrm{gran}}(\beta,\gamma)/\sin\beta\right) z\,\mathrm{d}S = L^3\, \boldsymbol{\Psi}_{\mathrm{gran}}(\beta,\gamma) \tag{4}$$

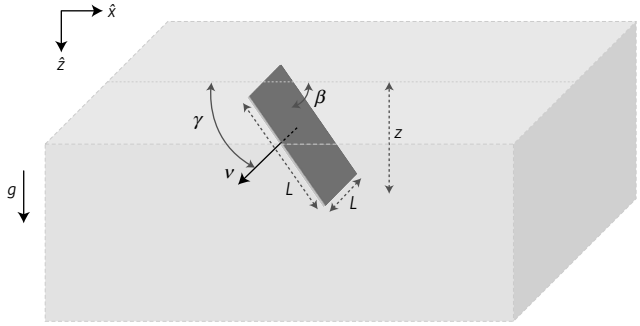

Figure 5 | Schematic of an RFT litmus test geometry. The 'garden hoe' geometry: An arbitrarily oriented square plate of side length L tilted at an angle β to the horizon in a semi-infinite domain of material. The plate's top edge is at the free surface. It is set into motion with speed v at an arbitrary angle γ to the horizon. Gravity, g, points downwards and the bottom of the plate is located at depth z.

This formula is precisely that of equation (3). Likewise, RFT hypotheses agree with full frictional-plastic continuum model solutions in the garden hoe family of geometries. Additionally, we see that gravity and density can be lumped as a scaling constant in the vector function $\mathbf{\Psi}_{\text{gran}}$. This prediction that all resistive force plots scale linearly in $\rho_c g$ for fixed friction constant(s) was validated in additional finite-element simulations.

For comparison, consider instead a viscous fluid, which obeys the Stokes equations, $\eta\partial^2 v_i/\partial x_j^2 - \partial P/\partial x_i + \rho g_i = 0, \partial v_i/\partial x_i = 0$, for dynamic viscosity η. For the same 'garden hoe' geometry described above, the intrusion force, $\mathbf{F}_{\text{visc}}$, must depend on β, γ, v, L and η. It cannot depend on ρg, as this term can be removed by absorbing it into the pressure in the Stokes equations without altering the resultant intruder force. We choose $L, L/v$ and $\eta L^2/v$ as the length, time and mass units, respectively, giving the dimensionless variables β, γ and $\mathbf{F}_{\text{visc}}/\eta L v$. Consequently, in viscous media, the force on the intruder must have the form $\mathbf{F}_{\text{visc}} = \eta L v\ \mathbf{\Psi}_{\text{visc}}(\beta, \gamma)$ for some vector-valued function $\mathbf{\Psi}_{\text{visc}}$. Absorbing the viscosity into $\mathbf{\Psi}_{\text{visc}}$, we have

$$\mathbf{F}_{\text{visc}} = L v\ \mathbf{\Psi}_{\text{visc}}(\beta, \gamma) \tag{5}$$

That the drag force grows linearly with L is similar to other Stokesian drag formulae; the drag on a sphere is proportional to its radius, for example.

We now compare the above form to a superposition-based solution, and determine if the two agree. (Unlike equation (1), the RFT of viscous fluids is historically an approximation developed for quasi-1D bodies only. To compare the effectiveness of frictional versus viscous superposition on surfaces, the analogous surface-level assumptions are considered here; we return to the 1D version of viscous RFT and compare to its frictional counterpart in Supplementary Section 2.) We suppose an isolated areal patch of small characteristic width λ oriented at various angles β and travelling at angles γ, and compute a local drag law. This takes the form $\{\text{Force/Area}\} = (a_x(\beta, \gamma), a_z(\beta, \gamma))v$ for some resistance coefficients a_x and a_z. The formula for viscous drag, equation (5), implies that $(a_x(\beta, \gamma), a_z(\beta, \gamma)) = \mathbf{\Psi}_{\text{visc}}(\beta, \gamma)/\lambda$. The total force is then estimated by superposition of the local drag rule over the surface of the macroscopic geometry:

$$\mathbf{F}_{\text{visc}}^{\text{RFT}} = \int_S \big(a_x(\beta, \gamma), a_z(\beta, \gamma)\big)\ v\,\mathrm{d}S = \frac{L^2}{\lambda} v\ \Psi_{\text{visc}}(\beta, \gamma) \tag{6}$$

The result scales as L^2, but this is not correct; per equation (5), the actual force scales as L. The disagreement implies that the surface-superposition principle is not precise for viscous fluids. The difference manifests due to a non-removable factor of λ, the selected micro-size, showing up in the local drag rule. The same issue arises in the common 1D application of RFT, used for slender bodies such as flagella and long microorganisms. In Supplementary Section 2, we explain how the accuracy of granular RFT continues in the limit of a slender body, while the viscous case, by contrast, retains this small-scale geometrical dependence, taking the form of a well-known logarithmically growing error.

Going beyond viscous fluids and frictional media, the garden hoe analysis can be applied diagnostically to arbitrary flow models to predict new RFTs in other materials. For example, consider a purely cohesional, rate-independent media, which can be modelled as a non-Newtonian fluid whose viscosity takes the form $\tau_y/\dot{\gamma}$ for some constant yield stress τ_y. Such a model describes the flow of certain gels[35], pastes[36], and muds[37] when strain rates are small enough to neglect dependence of flow stress on $\dot{\gamma}$. In this material model, the intruder force can depend only on β, γ, L and τ_y. We define L, L/v and $\tau_y L(L/v)^2$ as units of length, time and mass, respectively. Non-dimensionalizing, we find $\mathbf{F}_{\text{coh}} = \tau_y L^2\ \mathbf{\Psi}_{\text{coh}}(\beta, \gamma)$. Redefining $\mathbf{\Psi}_{\text{coh}}$ by absorbing the material constants, we obtain $\mathbf{F}_{\text{coh}} = L^2\ \mathbf{\Psi}_{\text{coh}}(\beta, \gamma)$. We now write cohesive RFT and check if it agrees with this relation. Applying the previous relation to a small plate with length λ, the force per area must obey $\mathbf{F}_{\text{coh}}/\lambda^2 = 2\mathbf{\Psi}_{\text{coh}}(\beta, \gamma)/\sin\beta \equiv (\alpha_x(\beta, \gamma), \alpha_z(\beta, \gamma))$. Superposing this local drag rule over the original $L \times L$ object gives

$$\mathbf{F}_{\text{coh}}^{\text{RFT}} = \int_S \big(\alpha_x(\beta, \gamma), \alpha_z(\beta, \gamma)\big)\,\mathrm{d}S = L^2 \mathbf{\Psi}_{\text{coh}}(\beta, \gamma) \tag{7}$$

The agreement between $\mathbf{F}_{\text{coh}}$ and $\mathbf{F}_{\text{coh}}^{\text{RFT}}$ means this material model has potential to possess a strong RFT. Our prediction is confirmed in V-intruder tests in Fig. 4c; the error of the RFT estimate, $|\mathbf{F} - \mathbf{F}_{\text{RFT}}|/|\mathbf{F}|$, is found to be 17% over the entire range orientations, and 2.8% when neglecting the orientations violating the leading-edge requirement (in grey). The RFT in cohesional media shown here has, to our knowledge, never previously been identified.

Outlook

The granular constitutive model we have used in this work was chosen to capture salient granular flow behaviours — a frictional, cohesionless constitutive relation — and we have shown that this bare description is sufficient to bring about RFT. Evidently there is more to the rheology of granular flow than these essential behaviours, and there are certainly limits where additional effects can become significant. Supplementary Section 3 provides more discussion on how inclusion of effects such as rate-sensitivity, nonlocality, or stress-dilatancy may influence the superposition results. However, because the two essential properties used in our approach are still the foundations of these more detailed constitutive approaches, any additional effects from these sources, for intrusion problems in the typical regimes discussed in this paper, should be within the margin of error between our theoretically obtained RFPs and the experimentally reported values in the literature.

The analysis in the 'garden hoe' geometry appears to have utility as a litmus test to discern which rheologies can have a strong RFT. Finite-element implementations verify the predictions made by this analytical method, as shown in Fig. 4. While it is certainly a necessary condition for strong RFT-type superposition in a material, the fact that RFT continues to work beyond the flat 'garden hoe' family, on surfaces with curves and kinks, may be related to hyperbolicity in the material's governing equations. For example, frictional (and cohesional) plasticity forms a hyperbolic system in space (in quasi-static 2D conditions), with stress characteristics extending from boundaries along 'slip-lines'[38]. This produces domains of dependence in the material such that stresses in certain zones can be attributed to the traction on a specific part of the surface of the intruder. This is in sharp contrast to viscous fluids, in which the equations are elliptic, and the stress at any point on an

object's surface is influenced by the motion and shape of the object's entire boundary.

In much the same way that the methods described herein have shown capable of predicting and confirming stronger or weaker RFTs in different materials, a major implication of the work is the possibility to identify new RFTs in other flowable materials when new applications arise. As the garden hoe analysis is straightforward to apply, we have noticed other problem set-ups that pass the test and would be worthy of further investigation, including intrusion in frictional-plastic substrates tilted at an incline to gravity, which could have implications in modelling sidewinding up granular inclines[39], and intrusion through inviscid fluids, which draws potential similarities with assumptions made in the Blade Element Theory of rotors[40]. By nature of the reconciliation of RFT with mechanics, reverting to the mechanical foundation could be a useful tool in determining RFT input data (RFPs) in circumstances difficult to measure experimentally, such as intrusion in micro-gravity. It is also possible, through study of the underlying mechanics, that broader versions of RFT may exist in more general interaction problems between structures and flowable media, beyond intrusion geometries.

Received 28 March 2016; accepted 13 July 2016; published online 29 August 2016; corrected online 11 October 2016

References

1. Dickinson, M. H. *et al*. How animals move: an integrative view. *Science* **288,** 100–106 (2000).
2. Vogel, S. *Life in Moving Fluids: The Physical Biology of Flow* (Princeton Univ. Press, 1996).
3. Lauder, G. V., Nauen, J. C. & Drucker, E. G. Experimental hydrodynamics and evolution: function of median fins in ray-finned fishes. *Integr. Comp. Biol.* **42,** 1009–1017 (2002).
4. Wang, Z. J. Dissecting insect flight. *Annu. Rev. Fluid Mech.* **37,** 183–210 (2005).
5. Li, C., Zhang, T. & Goldman, D. I. A terradynamics of legged locomotion on granular media. *Science* **339,** 1408–1412 (2013).
6. Thorpe, S. K., Holder, R. & Crompton, R. Origin of human bipedalism as an adaptation for locomotion on flexible branches. *Science* **316,** 1328–1331 (2007).
7. Biewener, A. A. Biomechanics of mammalian terrestrial locomotion. *Science* **250,** 1097–1103 (1990).
8. Bhushan, B. Biomimetics: lessons from nature–an overview. *Phil. Trans. R. Soc. A* **367,** 1445–1486 (2009).
9. Ma, K. Y., Chirarattananon, P., Fuller, S. B. & Wood, R. J. Controlled flight of a biologically inspired, insect-scale robot. *Science* **340,** 603–607 (2013).
10. Williams, B. J., Anand, S. V., Rajagopalan, J. & Saif, M. T. A. A self-propelled biohybrid swimmer at low Reynolds number. *Nat. Commun.* **5** (2014).
11. Ijspeert, A. J., Crespi, A., Ryczko, D. & Cabelguen, J.-M. From swimming to walking with a salamander robot driven by a spinal cord model. *Science* **315,** 1416–1420 (2007).
12. Maladen, R. D., Ding, Y., Li, C. & Goldman, D. I. Undulatory swimming in sand: subsurface locomotion of the sandfish lizard. *Science* **325,** 314–318 (2009).
13. Bekker, M. G. *Off-the-road locomotion: Research and Development in Terramechanics* (Univ. Michigan Press, 1960).
14. Meirion-Griffith, G. & Spenko, M. *Aerospace Conference, 2010 IEEE* 1–6 (IEEE, 2010).
15. Johnson, L. & King, R. Measurement of force to excavate extraterrestrial regolith with a small bucket-wheel device. *J. Terramechanics* **47,** 87–95 (2010).
16. Wong, J. Predicting the performances of rigid rover wheels on extraterrestrial surfaces based on test results obtained on earth. *J. Terramechanics* **49,** 49–61 (2012).
17. Uehara, J., Ambroso, M., Ojha, R. & Durian, D. Low-speed impact craters in loose granular media. *Phys. Rev. Lett.* **90,** 194301 (2003).
18. Shergold, O. A. & Fleck, N. A. *Proceedings of the Royal Society of London A: Mathematical, Physical and Engineering Sciences* Vol. 460**,** 3037–3058 (The Royal Society, 2004).
19. Gray, J. & Hancock, G. The propulsion of sea-urchin spermatozoa. *J. Exp. Biol.* **32,** 802–814 (1955).
20. Lighthill, J. *Mathematica Biofluiddynamics* (SIAM, 1975).
21. Lauga, E. & Powers, T. R. The hydrodynamics of swimming microorganisms. *Rep. Prog. Phys.* **72,** 096601 (2009).
22. Ding, Y., Gravish, N. & Goldman, D. I. Drag induced lift in granular media. *Phys. Rev. Lett.* **106,** 028001 (2011).
23. Maladen, R. D., Ding, Y., Umbanhowar, P. B., Kamor, A. & Goldman, D. I. Mechanical models of sandfish locomotion reveal principles of high performance subsurface sand-swimming. *J. R. Soc. Interface.* **8,** 1332–1345 (2011).
24. Rodenborn, B., Chen, C.-H., Swinney, H. L., Liu, B. & Zhang, H. Propulsion of microorganisms by a helical flagellum. *Proc. Natl Acad. Sci. USA* **110,** E338–E347 (2013).
25. Schofield, A. N. & Wroth, C. P. *Critical State Soil Mechanics* (McGraw-Hill, 1968).
26. Kamrin, K. Nonlinear elasto-plastic model for dense granular flow. *Int. J. Plast.* **26,** 167–188 (2010).
27. Kamrin, K. & Koval, G. Nonlocal constitutive relation for steady granular flow. *Phys. Rev. Lett.* **108,** 178301 (2012).
28. Henann, D. L. & Kamrin, K. A predictive, size-dependent continuum model for dense granular flows. *Proc. Natl Acad. Sci. USA* **110,** 6730–6735 (2013).
29. Chen, W.-F. *Limit Analysis and Soil Plasticity* (Elsevier, 2013).
30. Guillard, F., Forterre, Y. & Pouliquen, O. Depth-independent drag force induced by stirring in granular media. *Phys. Rev. Lett.* **110,** 138303 (2013).
31. Brzinski III, T., Mayor, P. & Durian, D. Depth-dependent resistance of granular media to vertical penetration. *Phys. Rev. Lett.* **111,** 168002 (2013).
32. Hill, R. New horizons in the mechanics of solids. *J. Mech. Phys. Solids* **5,** 66–74 (1956).
33. Dassault Systèmes Simulia, Providence, RI *Abaqus Reference Manuals* 6. 11 edn (2011).
34. Goldman, D. I. Colloquium: Biophysical principles of undulatory self-propulsion in granular media. *Rev. Mod. Phys.* **86,** 943–958 (2014).
35. Kinloch, I. A., Roberts, S. A. & Windle, A. H. A rheological study of concentrated aqueous nanotube dispersions. *Polymer* **43,** 7483–7491 (2002).
36. Senff, L., Labrincha, J. A., Ferreira, V. M., Hotza, D. & Repette, W. L. Effect of nano-silica on rheology and fresh properties of cement pastes and mortars. *Constr. Build. Mater.* **23,** 2487–2491 (2009).
37. Dzuy, N. Q. & Boger, D. V. Yield stress measurement for concentrated suspensions. *J. Rheol.* **27,** 321–349 (1983).
38. Nedderman, R. M. *Statics and Kinematics of Granular Materials* (Cambridge Univ. Press, 2005).
39. Marvi, H. *et al*. Sidewinding with minimal slip: Snake and robot ascent of sandy slopes. *Science* **346,** 224–229 (2014).
40. Adkins, C. N. & Liebeck, R. H. Design of optimum propellers. *AIAA Paper* 83–0190 (1983).

Acknowledgements

K.K. and H.A. gratefully acknowledge support from Army Research Office Grants W911NF-14-1-0205 and W911NF-15-1-0196.

Author contributions

K.K. conceived the study and supervised the project. H.A. developed the computational routines and conducted the numerical modelling. K.K. and H.A. jointly performed the analysis and wrote the paper.

Additional information

Supplementary information is available in the online version of the paper. Reprints and permissions information is available online at www.nature.com/reprints. Correspondence and requests for materials should be addressed to K.K.

Competing financial interests

The authors declare no competing financial interests.